

# Study on enhanced wear resistance of FeCoCrNi<sub>2</sub>MoSi high entropy alloy coatings induced by nano-layered eutectic and Laves phase

Di Chen<sup>a</sup>, Xiufang Cui<sup>a,\*</sup>, Yajie Guan<sup>a</sup>, Xinyao Li<sup>a</sup>, Sen Ma<sup>b</sup>, Zhongtao Dai<sup>a</sup>, Ziyu Song<sup>a</sup>, Litong Feng<sup>a</sup>, Guo Jin<sup>a,\*</sup>, Jinna Liu<sup>a,\*</sup>

<sup>a</sup> Key Laboratory of Superlight Material and Surface Technology of Ministry of Education, College of Material Science and Chemical Engineering, Harbin Engineering University, Harbin 150001, China

<sup>b</sup> AVIC Shenyang Aircraft Design & Research Institute, Shenyang 110035, China



## ARTICLE INFO

### Keywords:

Laser cladding  
High-temperature wear  
High entropy alloy coating  
Lamellar eutectics

## ABSTRACT

Wear is one of the primary challenges for high-temperature working components. In this paper, FeCoCrNi<sub>2</sub>MoSi eutectic high-entropy alloy coatings were successfully prepared by introducing MoNiSi ternary silicides with Laves structure into FeCoCrNi high-entropy alloys using laser cladding technology. The alloy achieves a balance of strength and toughness through the nanoscale eutectic structure with alternating FCC and Laves phases. Tribological experiments conducted over a wide temperature range from 25 °C to 800 °C show that the synergistic effect of the nano-lamellar structure and the alternating soft and hard structure makes the coating have excellent wear resistance at room temperature. The improvement of wear resistance at high temperatures (800 °C) is mainly due to the formation of the oxide film on the coatings.

## 1. Introduction

Surface damage to components caused by wear is a common issue in the advanced manufacturing industry that has a significant impact on the reliability and safety of equipment, as well as adding extra time and costs [1,2]. One of the most effective and economical ways to improve the wear resistance of materials is through surface engineering techniques [3–6]. The laser cladding technology is a popular choice for creating wear-resistant coatings on material surfaces due to its ability to achieve high deposition efficiency, controllable thickness, and high-quality metallurgical bonding. Consequently, it has garnered significant interest from researchers worldwide.

From a tribological perspective, numerous ternary metal silicide alloys possess a Laves phase crystal structure of the topologically closed packed (TCP) type (e.g., Mo<sub>2</sub>Ni<sub>3</sub>Si, Ti<sub>2</sub>Ni<sub>3</sub>Si, etc.) [7–10] and have demonstrated exceptional wear-resisting properties because of their high inherent hardness and strong anomalous hardness-temperature dependence. Additionally, the excellent metal adhesion resistance and antifriction of these silicides are attributed to the predominance of their covalent bonds.

These materials are suitable for many mechanical components operating under severe friction conditions as a new type of wear-

resistant materials. Nevertheless, the industrial application of these materials is limited by severe brittleness at room temperature and poor processability.

High entropy alloys (HEAs) have broadened the design possibilities of alloys by surpassing the constraints of traditional alloy materials, due to research and development from the perspective of entropy, as proposed by Yeh and Cantor [11,12]. HEAs with a face-centered cubic (FCC) crystal structure possess good ductility but poor strength, whereas those with a body-centered cubic (BCC) crystal structure exhibit excellent strength but low plasticity [13–15]. Therefore, based on the design concept of eutectic alloys, Lu et al. proposed high entropy eutectic alloys to achieve a balance between plasticity and strength [16]. The eutectic heterostructure of FCC and BCC (or Laves) phases aids in achieving both high strength and plasticity in EHEA [17–19]. The eutectic structure has attracted the attention of many scholars as an effective method to improve wear performance, and relevant studies have been carried out on the wear resistance of eutectic high entropy alloys [20–22]. It is found that the heterogeneous interfaces of alternating soft and hard densities in eutectic high entropy alloys provide excellent deformation resistance, and at the same time significantly enhance the wear resistance by uniformly withstanding the stresses [23–25]. However, the wear resistance of these alloys at high temperatures is slightly

\* Corresponding authors.

E-mail addresses: cuixf721@163.com (X. Cui), jinjg721@163.com (G. Jin), liujinna@hrbeu.edu.cn (J. Liu).

insufficient, which necessitates the development of new high-temperature wear-resistant EHEA coatings. Therefore, introducing ternary silicide with eutectic structures into HEA is a promising approach to optimizing the strength-ductility combinations of HEA while improving their tribological properties in high-temperature environments.

In this work, we have successfully prepared FeCoCrNi<sub>2</sub>MoSi EHEA coatings consisting of laves phase and FCC phase by introducing ternary metal silicide alloys with unusual hardness-temperature dependence and high hardness into HEAs using laser cladding technique, and exhibited uniform nano-lamellar eutectic structure. The high toughness property of the eutectic structure and the high-temperature property of the ternary silicide were used to synergistically enhance the frictional performance of EHEA, and the wear characteristics of the coatings at different temperatures, as well as the influence of the nanolayer structure on the wear resistance of the coatings, were systematically investigated.

## 2. Experimental

The FeCoCrNi<sub>2</sub>MoSi powder for laser cladding was prepared by mixing FeCoCrNi, Ni, Mo, and Si powders with a purity higher than 99.9% and an average particle size between 75 ~ 150  $\mu\text{m}$ . The raw powders were mixed in a planetary ball mill with a ball/powder mass ratio of 2:1 at a speed of 300 r/min for 0.5 h. They were then dried in a vacuum oven.

FeCoCrNi<sub>2</sub>MoSi EHEA coatings were fabricated on 38CrMoAl model steel using a continuous fiber laser cladding system that comprised a laser device (YLS-3000, IPG), a programmable robotic manipulator (KR30HA, KUKA) and an atmosphere protection device (AFS16). Firstly, the mixed EHEA powder with a nominal composition of FeCoCrNi<sub>2</sub>MoSi was pre-positioned on the surface of the 38CrMoAl substrate (100 mm × 100 mm × 10 mm), and the thickness of the pre-positioned layer was ~800  $\mu\text{m}$ . Argon is a protective gas in laser cladding processes. The parameters for cladding are displayed in Table 1.

The crystal structure of the EHEA coating was tested by a Philips Xpert-Pro X-ray diffractometer (XRD), operating at 40 KV voltage, 40 mA current, and a scanning rate of 5°/min. A scanning electron microscope (SEM, FEI Quanta 200) and transmission electron microscopy (TEM, FEI Talos F200x) were used to analyze the microstructure of the coatings. The elemental distribution of the coating was analyzed by an energy dispersive spectrometer (EDS). The sizes of the lamellae were determined via the conventional mean-linear-intercept method from SEM images. The SEM image was processed using the Image Pro and the phase ratio was determined by chromogenic methods.

The HV-1000A microhardness tester was used to measure the hardness of the coating cross-section with an applied load of 300 g and loaded for 15 s. Nano-mechanical properties of the coatings were analyzed using an Agilent G200 nano-indentation instrument. Each sample was tested 3 times to confirm the reliability of the results. Dry sliding friction experiments were carried out at room temperature (RT), 400 °C, and 800 °C for a duration of 60 min, using HT-1000 high-temperature friction and wear tester. The following tribological parameters were selected to investigate the effect of temperature on the tribological properties of EHEA based on the study of Du [24] and Deng [26] on the tribological properties of EHEA by load and velocity. Experimentally loaded with 2000 g, rotational speed 560 r/min, frequency 10 Hz, and friction radius 3 mm. The coating samples used for the sliding friction

experiments measured 15 mm × 15 mm × 10 mm and were produced using standard metallographic methods to achieve a surface roughness of less than 0.1  $\mu\text{m}$ . Al<sub>2</sub>O<sub>3</sub> ceramic balls with a diameter of 5 mm were used as counterparts due to their high hardness of 80 HRC, chemical inertness, and thermal resistance. Three parallel tests were performed on each sample under given tribological conditions. The wear rate of the coating is obtained by the formula  $W=V/(F \times S)$ , where W denotes the wear rate ( $\text{mm}^3 \cdot \text{N}^{-1} \cdot \text{m}^{-1}$ ), V denotes the amount of wear ( $\text{mm}^3$ ), F represents the load (N), and S is the relative slip distance between the friction pair and the sample (m). X-ray Photoelectron Spectrometer (XPS) from ThermoFisher Scientific was used to test the coating surface before and after a sliding friction experiment at 800 °C to determine the tribo-chemical mechanism.

## 3. Results and discussion

### 3.1. Microstructure characterization of FeCoCrNi<sub>2</sub>MoSi EHEA

**Fig. 2.** displays the XRD pattern of the FeCoCrNi<sub>2</sub>MoSi EHEA coating, which indicates that the EHEA consists of the Laves phase and FCC phase. To characterize the microstructure of the sample, we have analyzed the cross-sectional morphology of the material, as shown in **Fig. 3**, where **Figs. 3(b)** and **3(c)** show the backscattered electron (BSE) images of the microstructure of the EHEA coating and the interface between the coatings and the substrate, respectively, together with their corresponding EDS result. The microstructure of the coatings displays a characteristic lamellar eutectic structure, with alternating bands of greyish-white and greyish-black observed in **Fig. 3(b)**, the typical lamellar size of the eutectics is about 150 nm. The formation of lamellar structures is preferred when the volume fractions of the two eutectic phases are almost equal [27], as can be seen in **Fig. 3(d)**, where the ratio of the two phases is 42.9% and 57.1%, respectively. During the eutectic reaction, the Laves and FCC phases co-nucleate and grow while minimizing interfacial energy by maximizing the low-energy facets [28,29]. Meanwhile, from the EDS mapping and **Table 2**, it is intuitively clear that the grey-white phase is Mo-rich for the laves phase and the grey-black phase is Mo-poor for the FCC phase. The reason is that the larger atomic radius difference between Mo and Si elements and the extremely negative mixing enthalpy of Si elements with other elements make it more likely to form the intermetallic compound phase between Mo and Si elements, while the atomic radius difference and the mixing enthalpy of Fe, Co, Cr and Ni elements close to zero make it easier to form the FCC phase, which is consistent with the design of eutectic high entropy alloys containing non-metallic elements by Lu et al. [30].

In addition, the interface between the coating and the substrate (**Fig. 3(c)**) is clear, indicating that a strong metallurgical bonding interface was obtained between the coating and the substrate, and the coating interface shows a rough columnar crystal structure accompanied by a hypoeutectic structure dominated by a grey-black phase (FCC) and supplemented by grey-white streaks (Laves). The possible reasons for the formation of a hypoeutectic structure rather than a eutectic structure in the interface region are as follows: (1) During the laser cladding process, the heat of the molten pool is rapidly dissipated through the substrate along the direction perpendicular to the interface, and at the same time, in the interface region between the coating and the substrate, the molten pool is in direct contact with the substrate, which generates a large temperature gradient. The extremely fast cooling rate and high temperature gradient lead to the transformation of the lamellar eutectic structure in the interface region into a hypoeutectic structure and the formation of columnar grains. (2) The dilution effect of the laser cladding technology makes part of the Fe elements in the matrix diffuse to the interface region, which makes the elemental composition of the interface region deviate from the eutectic point, and generates subeutectic [31,32].

The lamellar eutectic structure (the coating region in **Fig. 3(a)**) was further characterized using scanning transmission electron microscopy

**Table 1**  
The parameters for cladding.

Powder	Power (W)	Scanning rate ( $\text{mm} \cdot \text{s}^{-1}$ )	Spot diameter (mm)	Overlap rate
FeCoCrNi <sub>2</sub> MoSi	1500	25	3	30% ~40%

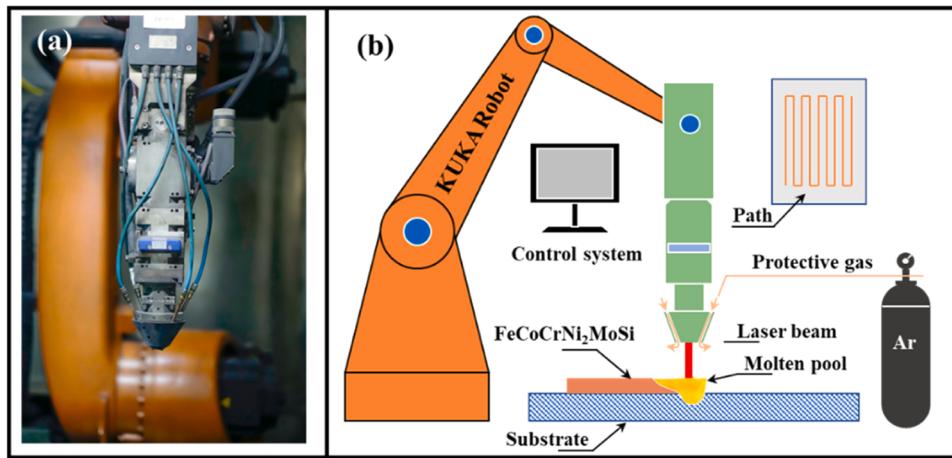


Fig. 1. Schematic diagram of laser cladding system.

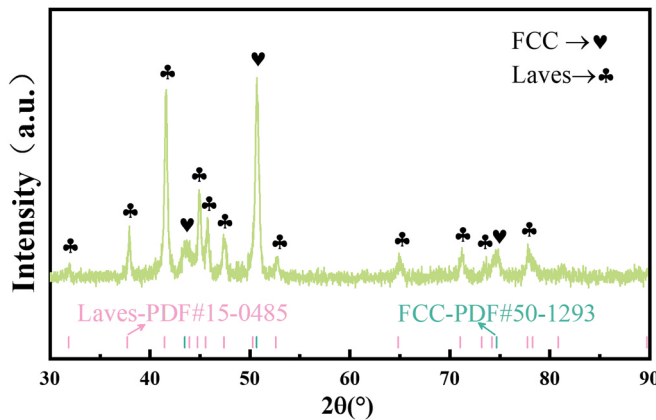


Fig. 2. The XRD pattern of the EHEA coating.

(STEM), Fig. 4(a) shows a high-angle annular dark field (HAADF) STEM micrograph, the two-phase alternating nanosheet laminar structure as well as the smooth and curved laminar interface between the two phases can be clearly observed. The previous study indicates that this nanosheet laminar structure possesses high strength and toughness [18,33]. As a result, it can mitigate stress concentration during the friction process.

The corresponding maps for selected area electron diffraction (SAED) (Fig. 4(c)-Fig. 4(d)) show that the eutectic biphasic phase consists of an FCC phase along the [011] zone axis and a Laves phase along the [12̄13] zone axis. Additionally, the corresponding EDS spectra reveal that the dark grey phase consists of the FCC phase with Fe, Co, Cr, and Ni as the main component and the Mo-rich bright grey phase corresponds to the Laves phase.

To study the correlation between the two phases in eutectic structure, we analyzed the interface between the FCC and Lave phases, as shown in the high-resolution transmission electron microscopy (HRTEM) image (Fig. 5(a)). The interfacial smoothness at the nanoscale between the two phases is manifested as a distribution of discrete atomic steps along the phase interface due to the lower or higher solid solution entropy in the solidification process, which is the typical morphology of the non-faceted eutectic growth [33–35]. By quantitative analysis, the

**Table 2**  
Statistics of element content of the FeCoCrNi<sub>2</sub>MoSi EHEA.

Area	Composition (at%)					
	Fe	Co	Cr	Ni	Mo	Si
Overall	23.40	12.94	14.11	25.98	13.05	10.52
FCC	25.08	13.27	16.36	30.17	6.27	8.85
Laves	22.55	13.21	14.35	25.58	13.24	11.06

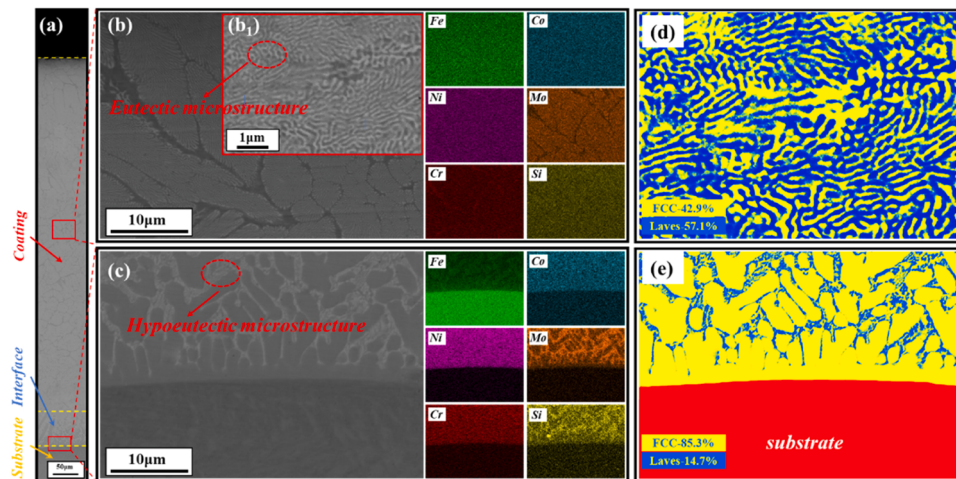
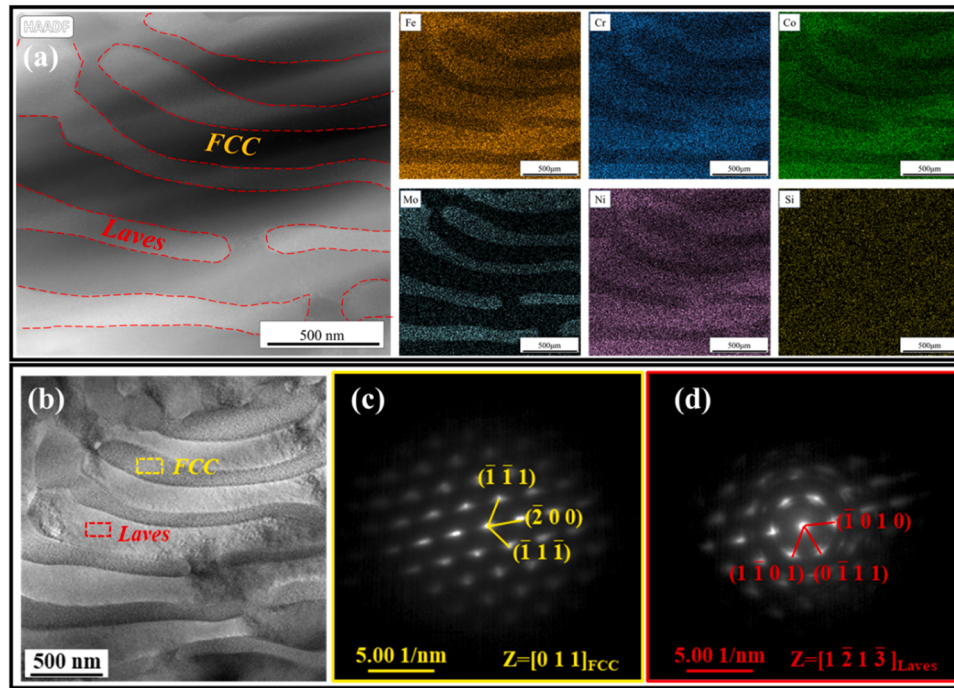


Fig. 3. Cross-section structures and phases of the EHEA coating. (a) the overall SEM image of the macroscopic coating (b-c) The coating and interface sections of the EHEA; (d-e) the phases proportion of the coating and interface.



**Fig. 4.** STEM images and elemental distribution diagrams of FeCoCrNiMo<sub>2</sub>Si EHEA coating. (a) HAADF-STEM image showing the alternating dual-phase lamellae; (b) the low magnification TEM image of the dual phase. (c) the SAED pattern of the Laves phase, (d) the SAED pattern of the FCC phase.

crystal plane distance  $d_{(1\bar{1}\bar{1})} = 0.204 \text{ nm}$  for the FCC phase, and the crystal plane spacing  $d_{(0\bar{1}11)} = 0.238 \text{ nm}$  for the Laves phase. This is in agreement with the lattice constants that have been determined by XRD. In addition, we have identified a specific orientation relationship, i.e.  $[011]_{\text{FCC}} // [1\bar{2}1\bar{3}]_{\text{Laves}}$ . Besides, the angle of orientation mismatch between the close-packed planes of the FCC phase and the Laves phase is approximately  $22.95^\circ$ . As a result, the parameter of mismatch between the two phases is calculated via the formula  $\sigma = \frac{0.238\text{nm}-0.204\text{nm}/\cos(22.95^\circ)}{0.204\text{nm}/\cos(22.95^\circ)} \sim 0.0743$  [33], suggesting a semi-coherent interface between the two phases. A cluster of dislocations caused by lattice mismatch can be observed at the interface between the FCC and Laves phases. This is demonstrated in the FFT filtered image (Fig. 5 (g)).

### 3.2. Phase formation

Thermophysical parameters such as  $\Delta S_{\text{mix}}$  (entropy of mixing),  $\Delta H_{\text{mix}}$  (enthalpy of mixing), VEC (valence electron concentration), and  $\delta$  (atomic size difference) are considered to be a predictor of the crystal structure of HEAs, and the relationship between the phase and the thermophysical parameters has been explored by many researchers. Hence, for further validation of the phase structure of the coating microstructure,  $\Delta S_{\text{mix}}$ ,  $\Delta H_{\text{mix}}$ , VEC, and  $\delta$  were employed. The thermodynamic parameters were calculated using equations (1), (2), (3), and (4). The parameters required for the calculation are given in Table 3 and Fig. 6 [36,37].

$$\Delta S_{\text{mix}} = -R \sum_{i=1}^n c_i \ln c_i$$

$$\Delta H_{\text{mix}} = \sum_{i=1, i \neq j}^n \Omega_{ij} c_i c_j$$

$$\delta = 100 \sqrt{\sum_{i=1}^n c_i \left(1 - \frac{r_i}{\bar{r}}\right)^2}$$

$$\text{VEC} = \sum_{i=1}^n c_i (\text{VEC})_i$$

Where R is the gas constant,  $\Omega_{ij} = 4\Delta_{\text{mix}}^{AB}$ ,  $\Delta_{\text{mix}}^{AB}$  is the mixing enthalpy of binary liquid AB alloys,  $\bar{r} = \sum_{i=1}^n c_i r_i$ ,  $c_i$  and  $r_i$  are the atomic percentage and atomic radius of the  $i$ th element, respectively.

Kim and Chanda et al. [38,39] used  $\delta$ -VEC and  $\delta$ - $\Delta H_{\text{mix}}$  diagrams to assess the trend of phase formation in various HEAs, EHEAs form within regions of the green box in Fig. 7, where  $-18 \leq \Delta H_{\text{mix}} \leq -6$ ,  $6 \leq \text{VEC} \leq 8.5$ , and  $\delta > 3$ . Moreover, EHEAs with FCC+TCP phases tend to form when the VEC is between 7.5 and 8.5, and EHEAs with BCC+TCP phases tend to form when the VEC is between 6 and 7.5, as illustrated by the two dashed ellipses in Fig. 7(b). Hence, it is apparent from Fig. 7 that the FeCoCrNi<sub>2</sub>MoSi EHEA fits both empirical criteria and tends to form a eutectic structure with the FCC/Laves phase, a tendency which is also consistent with the current experimental results.

### 3.3. Micro-hardness and nano-hardness

Fig. 8 displays the micro-hardness of FeCoCrNi<sub>2</sub>MoSi EHEAs measured by Vickers hardness tester at room temperature (RT). The uniformity of the EHEA structure is evidenced by the smooth micro-hardness curves. The average micro-hardness of the EHEAs was calculated as  $594.1 \pm 3 \text{ HV}$ . The coatings' micro-hardness primarily originates from solid solution strengthening and the mutual reinforcing effect of Laves intermetallic compounds. Furthermore, the coatings consist of Fe, Co, Cr, Ni, Mo, and Si elements with a large difference in atomic radii, resulting in substantial lattice distortions that augment the solid solution strengthening effect [40–42]. As Si possesses a smaller atomic radius than the other elements present in the alloy, it reduces the mobility of the dislocations and increases the strain energy, thus increasing the solid solution strengthening effect [43].

To precisely ascertain the mechanical characteristics of the distinct micro-regions, nanoindentation assessments were performed on the FCC and Lave phases. Our analysis revealed that the FCC and Laves phases have a hardness of 4.83 and 6.08 GPa, respectively, as shown in Fig. 9

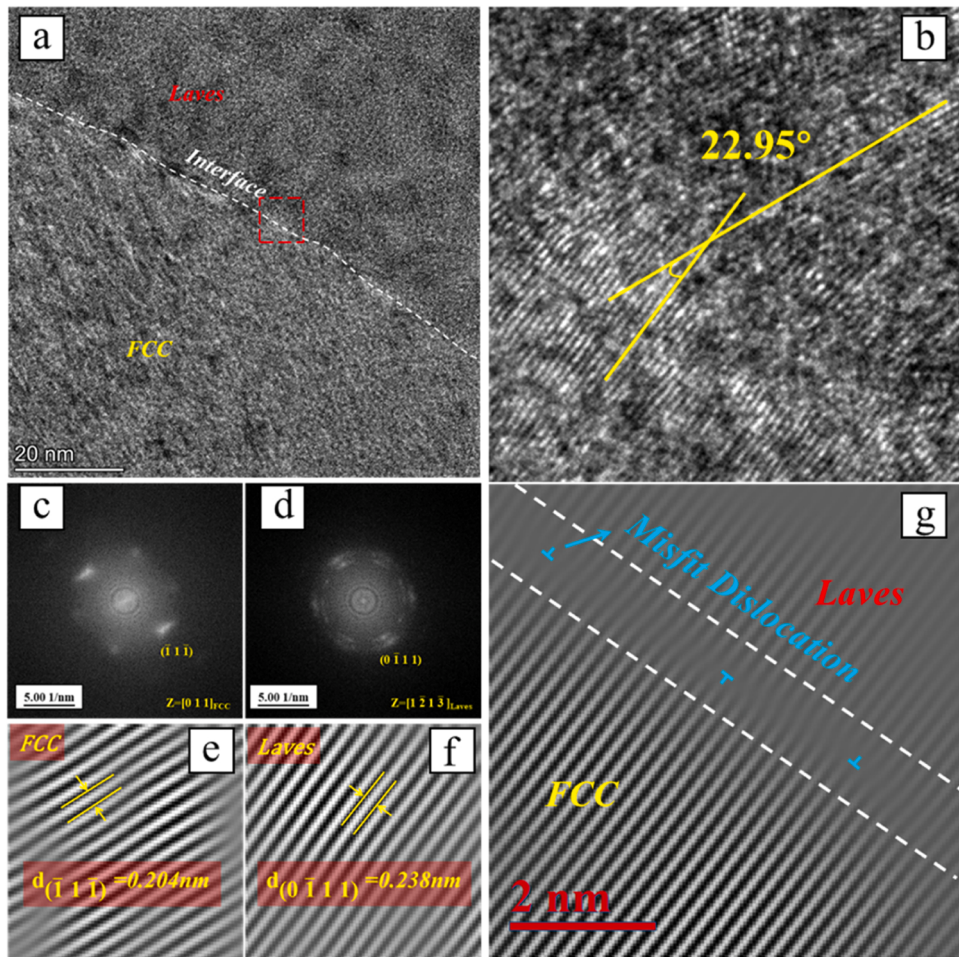


**Fig. 5.** Phase-interface characteristics at an atomic scale. (a) HRTEM image of the Laves and FCC phases, (b) Fast Fourier Transformation (FFT) and (g) Inverse FFT (IFFT) images of the marked region in (a), the FFT filtered images of (c) the FCC phase, (d) the laves phase, the IFFT filtered images of (e) the FCC phase, (f) the laves phase.

**Table 3**

Corresponding parameters of alloying elements in FeCoCrNi<sub>2</sub>MoSi EHEA.

Elements	Atomic radius/Å	VEC	Mixing enthalpy (kJ·mol <sup>-1</sup> )					
			Fe	Co	Cr	Ni	Mo	Si
Fe	1.241	8	—	-1	-1	-2	-2	-35
Co	1.251	9	—	—	-4	0	-5	-38
Cr	1.249	6	—	—	-7	0	-37	
Ni	1.246	10	—	—	—	-7	-40	
Mo	1.363	3	—	—	—	—	-35	
Si	1.153	11	—	—	—	—	—	

**Table 4**

The  $\delta$ ,  $\Delta S_{\text{mix}}$ ,  $\Delta H_{\text{mix}}$ , and VEC of FeCoCrNi<sub>2</sub>MoSi EHEA.

Alloys	$\delta$ (%)	$\Delta S_{\text{mix}}$ (J/K·mol)	$\Delta H_{\text{mix}}$ (kJ·mol <sup>-1</sup> )	VEC
EHEA	6.47	14.41	-17.59	7.68

and Table 5. The Young's modulus of the FCC and Laves phases are 208.4 and 208.6 GPa, respectively. Notably, the FCC phase exhibits lower elasticity (577.3 PJ) and higher plasticity (3054.4 PJ). The findings suggest that the Laves phase displays increased hardness and resistance to deformation, whereas the FCC phase exhibits greater susceptibility to plastic deformation. Furthermore, synergistic effects during friction may be induced by the alternative structures with both soft and hard heterogeneity in two phases.

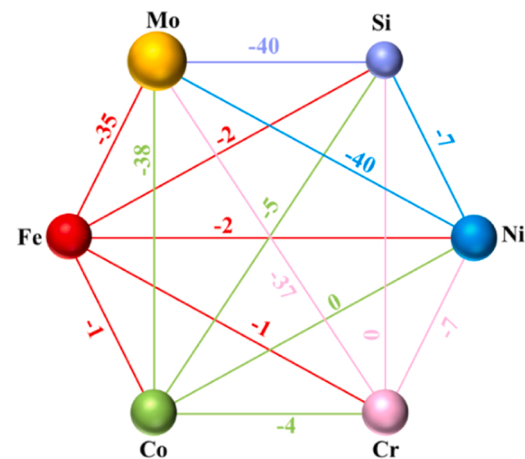


**Fig. 6.** Values of  $\Delta H_{\text{mix}}^{\text{AB}}$  in FeCoCrNi<sub>2</sub>MoSi EHEA system.

The plasticity index of a material is expressed as  $\varphi$  ( $\varphi = \frac{E}{H} \left( \frac{\delta}{\beta} \right)^{\frac{1}{2}}$ ) [44, 45]. Where  $\delta$  represents the surface roughness,  $\beta$  denotes the roughness radius. Showing that  $\frac{E}{H}$  is proportional to  $\varphi$ , Table 5 summarizes the calculated values, which indicates that the  $\frac{E}{H}$  is greater for FCC, i.e. the plasticity index is higher, which means that plastic deformation tends to

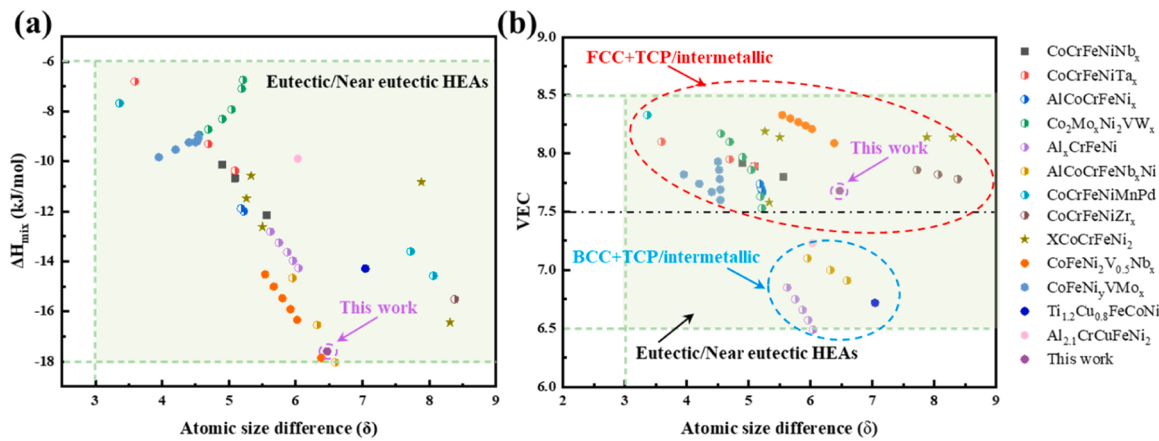


Fig. 7. The Relationships between (a)  $\Delta H_{\text{mix}}$  and  $\delta$ , (b) the VEC and  $\delta$  for the FeCoCrNi<sub>2</sub>MoSi EHEA and typically-reported EHEAs [39].

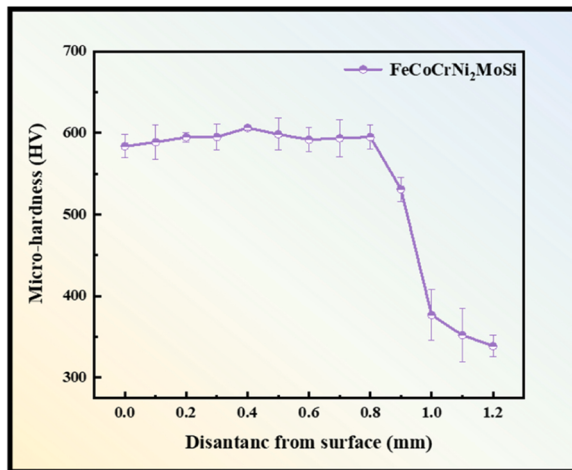


Fig. 8. Micro-hardness curve of FeCoCrNi<sub>2</sub>MoSi EHEA coating.

occur at the FCC phase. Furthermore, on the basis of the Hertz contact theory of balls in a plane, it is possible to give a limiting expression for the normal load  $N$  ( $N < 5.618\alpha^3 R^2 \frac{H^3}{E^2}$ ) in the absence of appreciable plastic deformation, where  $\alpha$  is a constant and  $R$  is the radius of the contacting ball. As shown in Table 5, the Laves phase with higher  $\frac{H^3}{E^2}$  is able to withstand higher contact with normal loads. From the comprehensive analysis, it is known that the Laves phase is hard but brittle, and the FCC phase has a low yield strength but excellent deformation capacity [46,47].

#### 3.4. Tribological performance of FeCoCrNi<sub>2</sub>MoSi EHEA at different temperatures

Fig. 10 shows the wear performance of FeCoCrNi<sub>2</sub>MoSi EHEA at different temperatures in a dry sliding test. As shown in Fig. 10(a), the relationship between the coefficient of friction (COF) and wear time indicates that the COF decreases from 0.43 at room temperature (RT) to 0.20 at 800 °C. The wear rate of the eutectic high-entropy alloy at different temperatures (As shown in Fig. 10(d)) calculated from the wear area obtained from the analysis of the cross-sectional profile of the wear trajectory in Fig. 10(b) shows a similar trend, e.g., the wear rate decreases from  $3.92 \times 10^{-5}$  to  $1.09 \times 10^{-5} \text{ mm}^3 \cdot \text{N}^{-1} \cdot \text{m}^{-1}$  at 800 °C. This may be related to the oxide coverage of the alloy surface, resulting in a lower coefficient of friction and wear rate [48]. In addition, the COF curve shows a typical form of sawtooth fluctuation, with large wear fluctuations at RT. The fluctuations in sawtooth waves can be attributed

to two primary reasons. For one thing, it is caused by the periodic accumulation and elimination of hard debris dropped during wear [49], and for another, the hardness of the Laves phase is inconsistent with that of the FCC phase, and the grinding ball continues to pass through the two phases during friction, which leads to inconsistent cutting resistance. The findings show that the wear resistance of the FeCoCrNi<sub>2</sub>MoSi EHEA is significantly improved with increasing temperature.

To investigate the complex influence of microstructure on the wear mechanism during dry sliding tests at different temperatures, Fig. 11 shows the corresponding wear surfaces with elemental distribution. As shown in Fig. 11(a<sub>2</sub>), on the wear surface at RT, wear debris of larger size and wide hook grooves parallel to the sliding direction were observed. Meanwhile, the EDS result shows that the content of element O in the sample is 22.95 at%, with uneven distribution on the wear surface, primarily in the abrasive chips. This uneven distribution is attributed to the constant extrusion and deformation of the abrasive chips during the friction process, as well as oxidation after heating. These observations indicate that the wear mechanism of FeCoCrNi<sub>2</sub>MoSi EHEA at RT is adhesive wear with abrasive wear accompanied by slight oxidation. As the experimental temperature increases, it is clear from Fig. 11 (b<sub>2</sub>) and (b<sub>3</sub>) that the wear mechanism of the coatings changes, with the EHEA coatings showing many patches of oxide in the 400 °C wear test, and the patches forming an oxide layer that protects almost the entire wear surface when the temperature rises to 800 °C, as shown in Fig. 11(c<sub>2</sub>), demonstrates the transition from periodic oxide fragments to glaze-layer (also known as an oxide layer). The formation of a patchy structure may be due to the generation and adhesion of debris and oxides during the elevated temperature friction experiments, and thus a large number of debris may be formed during cyclic friction, as shown in Fig. 11(b<sub>2</sub>). Previous studies have shown that the formation of the flake structure reduces friction and protects the surface from abrasion [50–53]. As a result, the wear surface after the 800 °C friction test is smoother, with less wear debris and a lower wear rate.

With the increase of the experimental temperature, the elemental distribution of the wear tracks is shown in Fig. 11 ((b<sub>3</sub>) - (c<sub>3</sub>)) and Table 6, which also demonstrates the O element has a homogeneous distribution at 800 °C, which indicates that a complete oxide film is generated during the wear process. To sum up, the wear mechanisms of the FeCoCrNi<sub>2</sub>MoSi eutectic high-entropy alloy at 400 °C comprise adhesive wear, delamination wear, and oxidative wear. As the temperature increases to 800 °C, the wear mechanisms are mainly oxidative wear and delamination wear.

Fig. 12 shows the comparison of tribological properties of FeCoCrNi<sub>2</sub>MoSi with other high entropy alloys at RT. Fig. 13 shows the schematic diagram of the wear mechanism. It is clear from Fig. 12 that the EHEA exhibits excellent wear resistance at room temperature. From previous reports, it is known that the high strength and ductility of the

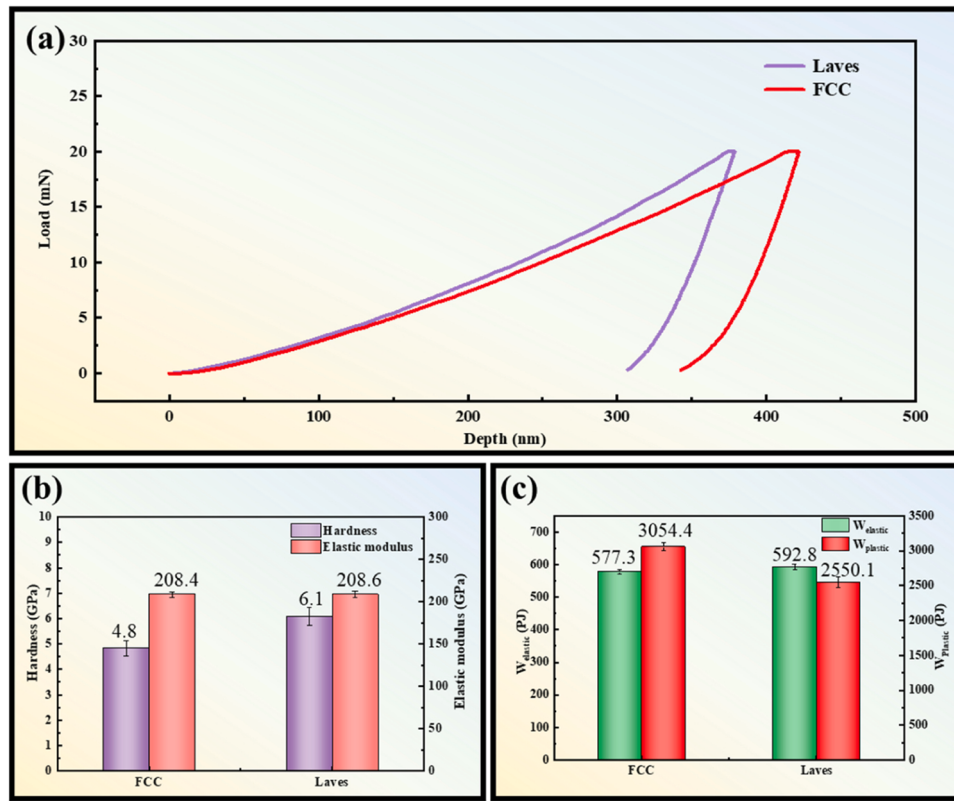


Fig. 9. Nanoindentation tests of FCC/Laves phases. (a) load-displacement curve, (b) hardness and Young's modulus, (c)  $W_{\text{elastic}}$  and  $W_{\text{plastic}}$ .

Table 5

Nanoindentation test results of the Laves phase and the FCC phase.

Region	E (GPa)	H (GPa)	$W_{\text{elastic}}$ (PJ)	$W_{\text{plastic}}$ (PJ)	H/E	$H^3/E^2$
FCC	208.4	4.8	577.3	3054.4	0.023	0.0026
Laves	208.6	6.1	592.8	2550.1	0.029	0.005

lamellar structure are attributed to (i) the large amount of dislocations movement in the FCC (soft) phase, (ii) the synergistic effect of dislocations blocking at the soft/hard layer boundary [54,55]. Additionally, the strength factor (K) at the crack tip is one of the important factors affecting the microcrack extension in the Laves phase based on the fracture mechanics criterion [24], with  $K = \sigma\sqrt{\pi}h$ , where h represents the size of the brittle grain/layer. When h is very small, it becomes more difficult to extend microcracks in the Laves phase. Thus, in FeCoCrNi<sub>2</sub>-MoSi EHEA with nanolaminates, the confinement of the Laves phase on a nanoscale through the creation of a high-density heterogeneous interface can greatly enhance the toughness of the lamellar eutectic [24, 56–58]. When the layer thicknesses of both materials contract to the nanoscale range (<500 nm), the uniform co-deformation of the lamellar structure effectively reduces the stress concentration that may occur in the primary phase of sub-eutectic or per-eutectic microstructures [59]. Consequently, nano-lamellar FeCoCrNi<sub>2</sub>-MoSi eutectics EHEA display exceptional wear resistance in RT friction experiments.

The formation of a protective glaze-layer during high-temperature wear is an important feature in reducing the wear of metal alloys because it prevents direct contact between the pin and disc and also has a lubricating effect. The formation and properties of the glaze-layer are influenced by the temperature and the Microstructure of the alloy itself and affect the wear process. Additionally, the glaze-layer is continuously damaged and produced throughout the wear process, resulting in a dynamic equilibrium between the constantly exposed metal surface and the oxide layer produced by the high temperature reaction [72,73].

Apart from the protection of the glaze-layer, the influence of the microstructure beneath the oxide surface plays a key role in the wear behavior. As in the case of friction in room temperature environment, the nanoscale Laves phase and FCC are bound to each other to achieve a uniform co-deformation of materials with different softness and hardness, which serves as the skeleton of the coating as a whole, and thus improves the overall high-temperature wear resistance of the coating.

In order to accurately analyze the types of oxides formed by FeCoCrNi<sub>2</sub>-MoSi coatings during high temperature friction and to detect the valence of the oxidation products, the results of the XPS of the FeCoCrNi<sub>2</sub>-MoSi EHEA before and after a sliding friction experiment at 800 °C are shown in Fig. 14. As shown in Fig. 14, based on the XPS spectra fitted in the binding energy range of 700–749 eV, it is possible to distinguish different peaks at 711.4 and 723.5 eV, which correspond to the Fe<sub>2</sub>O<sub>3</sub> [74,75]. In the Co<sub>2p</sub> spectrum, the peaks at 780.5 and 796.1 eV are associated with the Co oxides CoO and Co<sub>2</sub>O<sub>3</sub>, while the peak at 782.2 eV is associated with the inorganic acid salt CoCrO<sub>4</sub> [24, 74]. Meanwhile, by deconvolution of the Cr<sub>2p</sub> peaks, the Cr<sub>2p</sub> peak at 576.1 eV corresponds to the inorganic acid salt NiCr<sub>2</sub>O<sub>4</sub>, while the peak positions at 578.1 and 585.9 eV belong to Cr<sub>2</sub>O<sub>3</sub> [74,75]. Analysis of the Ni peaks shows that various lubricating nickel oxides Ni<sub>x</sub>O<sub>y</sub> (NiO, Ni<sub>2</sub>O<sub>3</sub>) appear on the wear surface, which contributed to the reduction of the coefficient of friction under high temperature wear [53,74]. The presence of MoO<sub>3</sub>, SiO<sub>2</sub> and SiO is also confirmed in the spectra of Mo<sub>3d</sub> with Si<sub>2p</sub> [74,76]. In summary, dry sliding friction experiment at 800 °C leads to complete oxidation and the formation of inorganic acid salts, which form a dense oxidised friction layer with good wear resistance.

#### 4. Conclusions

In conclusion, we have successfully developed FeCoCrNi<sub>2</sub>-MoSi EHEA coatings in this work and investigated the microstructure, mechanical properties, and tribological properties of the EHEA coatings. The dry sliding wear behaviors of the coating at different temperatures (25 ~

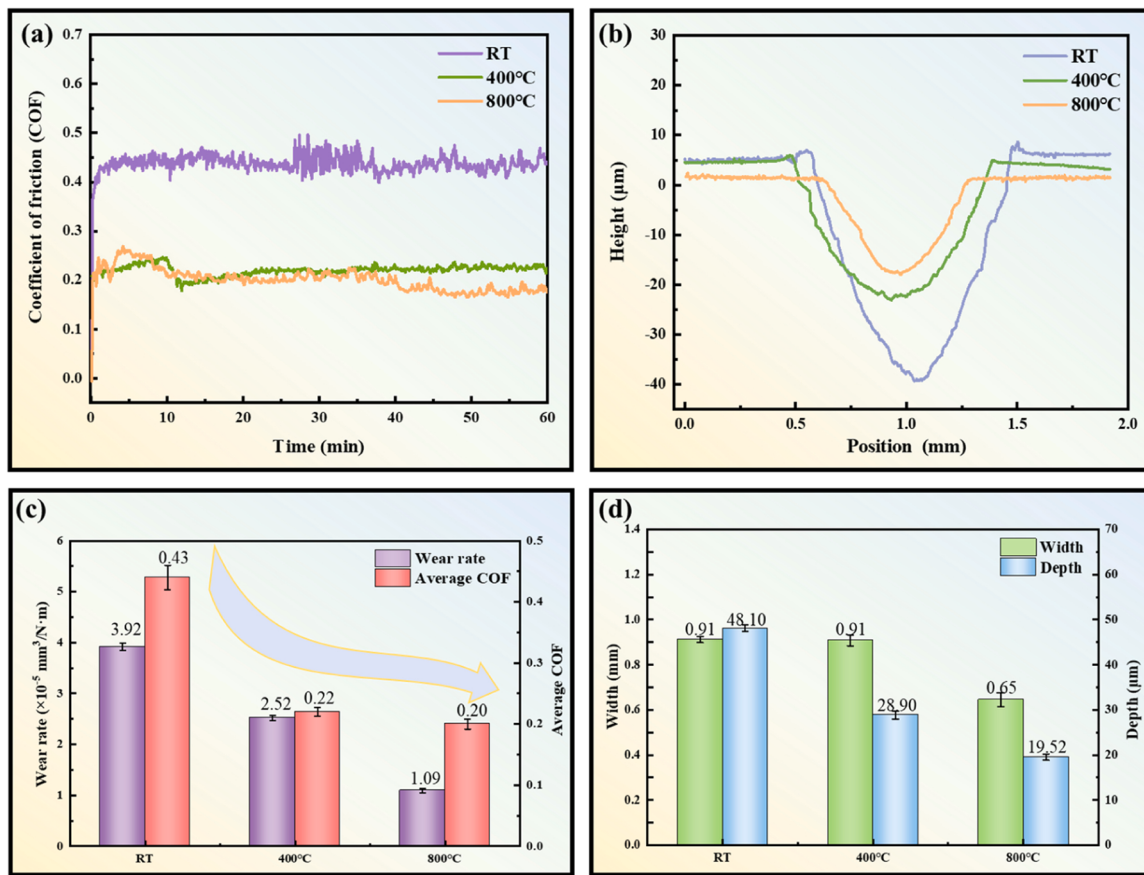


**Fig. 10.** Tribological performance of FeCoCrNi<sub>2</sub>MoSi EHEA coating. (a) COF of for each temperature, (b) wear track section curve, (c) steady-state average COF and wear rate for each temperature, (d)width and depth of each wear track.

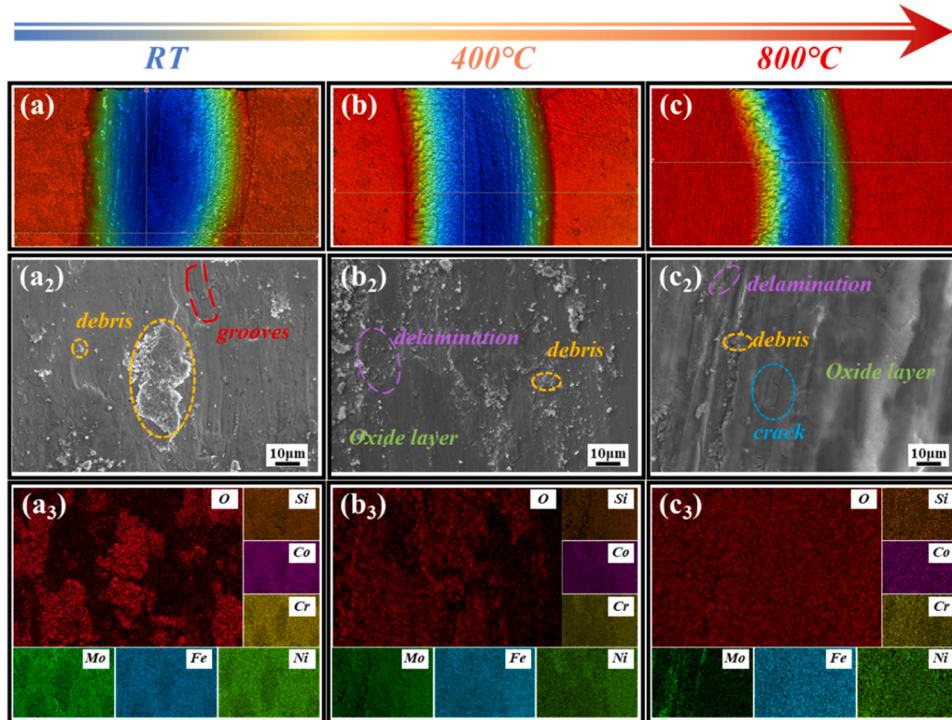


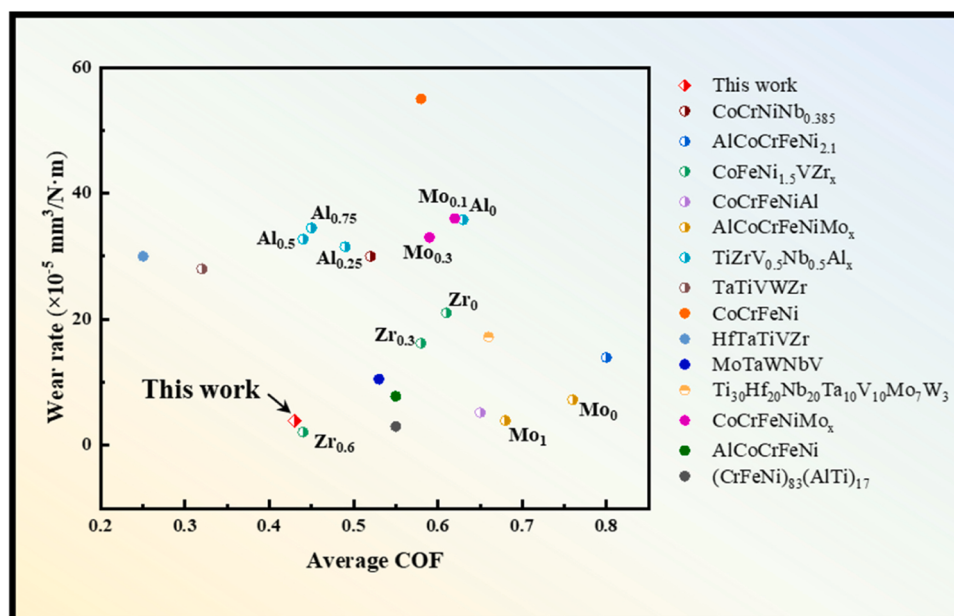
**Fig. 11.** Three-dimensional morphology, SEM images and correlated EDS mapping of worn surfaces at ((a<sub>1</sub>) - (a<sub>3</sub>)) RT, ((b<sub>1</sub>) - (b<sub>3</sub>)) 400 °C, ((c<sub>1</sub>) - (c<sub>3</sub>)) 800 °C.

**Table 6**  
Element composition (at%) of the worn surfaces at different temperatures.

Temperature	Composition (at%)						
	O	Fe	Co	Cr	Ni	Mo	Si
RT	22.95	17.7	10.19	10.65	19.86	9.86	22.95
400 °C	32.54	22.09	7.94	8.37	15.4	6.73	6.93
800 °C	52.95	21.64	4.97	6.12	8.39	1.12	4.81

**Table 7**Comparison of tribological properties of FeCoCrNi<sub>2</sub>MoSi with other reported high entropy alloys at room temperature.

HEA	Structure	Average COF	Wear rate ( $\times 10^{-5} \text{ mm}^3 \cdot \text{N}^{-1} \cdot \text{m}^{-1}$ )	Ref.
FeCoCrNi <sub>2</sub> MoSi	FCC+ Laves (eutectic)	0.43	3.92	This work
CoCrNiNb <sub>0.385</sub>	FCC+ Laves (eutectic)	0.52	30.0	[25]
AlCoCrFeNi <sub>2.1</sub>	FCC+BCC (eutectic)	0.8	13.94	[60]
CoFeNi <sub>1.5</sub> V	FCC	0.61	21.01	[61]
CoFeNi <sub>1.5</sub> VZr <sub>0.3</sub>	FCC+ Laves (hypoeutectic)	0.58	16.2	[61]
CoFeNi <sub>1.5</sub> VZr <sub>0.6</sub>	FCC+ Laves (hypoeutectic)	0.44	2.13	[61]
CoCrFeNiAl	FCC+ $\sigma$	0.65	5.2	[62]
AlCoCrFeNi	FCC+ BCC	0.76	7.21	[63]
AlCoCrFeNiMo	FCC+ $\sigma$	0.68	3.92	[63]
TiZrV <sub>0.5</sub> Nb <sub>0.5</sub>	BCC	0.63	35.8	[64]
TiZrV <sub>0.5</sub> Nb <sub>0.5</sub> Al <sub>0.25</sub>	BCC+ Laves	0.49	31.5	[64]
TiZrV <sub>0.5</sub> Nb <sub>0.5</sub> Al <sub>0.5</sub>	BCC+ Laves	0.44	32.7	[64]
TiZrV <sub>0.5</sub> Nb <sub>0.5</sub> Al <sub>0.75</sub>	BCC+ Laves	0.45	34.5	[64]
TaTiVWZr	BCC+BCC	0.32	28.0	[65]
CoCrFeNi	FCC	0.58	55.0	[66]
HfTaTiVZr	BCC	0.25	30.0	[65]
MoTaWNbV	BCC	0.53	10.5	[67]
Ti <sub>30</sub> Hf <sub>20</sub> Nb <sub>20</sub> Ta <sub>10</sub> V <sub>10</sub> Mo <sub>7</sub> W <sub>3</sub>	BCC	0.66	17.2	[68]
CoCrFeNiMo <sub>0.1</sub>	FCC	0.62	36	[69]
CoCrFeNiMo <sub>0.3</sub>	FCC	0.59	33	[69]
AlCoCrFeNi	FCC+B2 + $\sigma$	0.55	7.78	[70]
(CrFeNi) <sub>83</sub> (AlTi) <sub>17</sub>	FCC+BCC+L2 <sub>1</sub>	0.55	3.0	[71]

Fig. 12. Comparison of tribological properties of FeCoCrNi<sub>2</sub>MoSi with other high entropy alloys at RT.

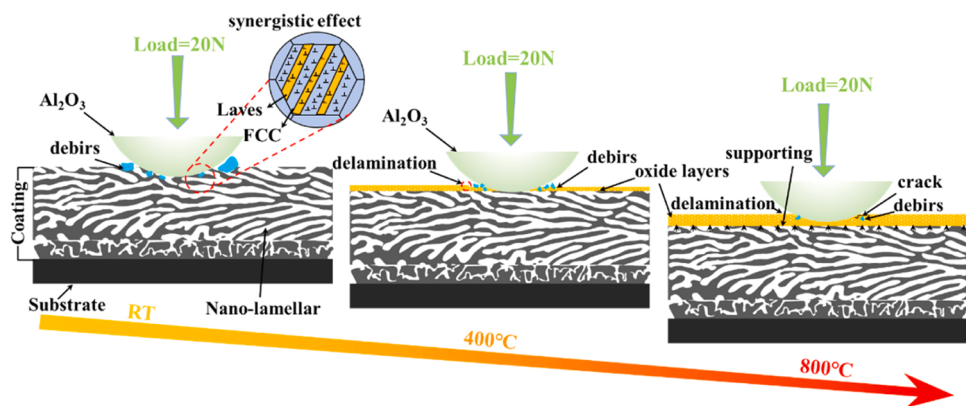


Fig. 13. The schematic diagram of the wear mechanism.

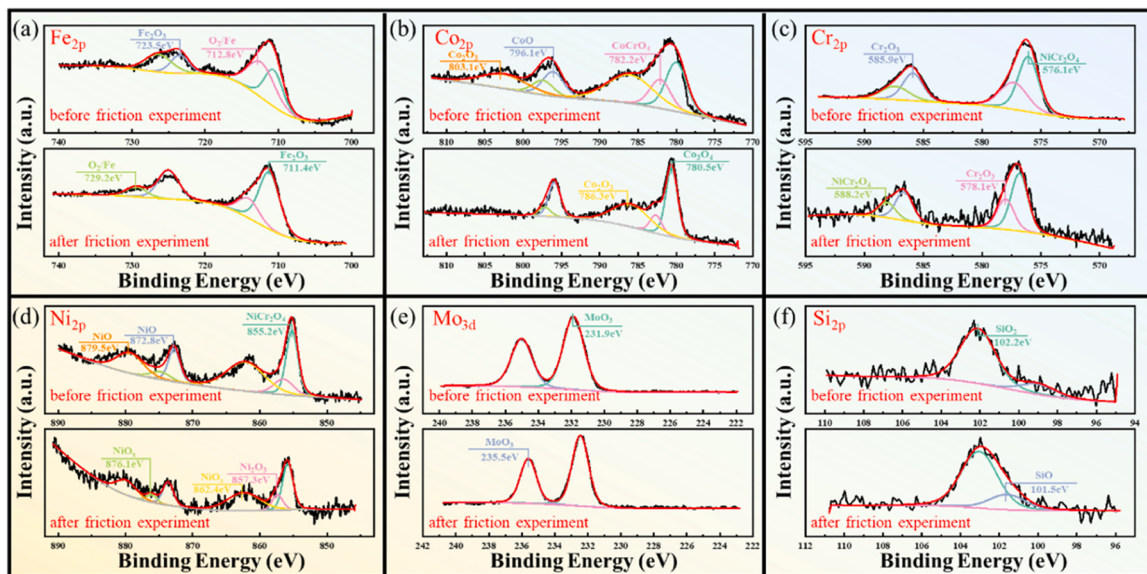


Fig. 14. XPS spectrum of FeCoCrNi<sub>2</sub>MoSi EHEA before and after friction experiment at 800 °C.

room temperature are adhesive wear and abrasive wear, and as the temperature increases, the wear mechanisms gradually change to oxidative wear and delamination wear, so that the coefficient of friction and the wear rate are the lowest at 800 °C, which are 0.20 and  $1.09 \times 10^{-5} \text{ mm}^3 \cdot \text{N}^{-1} \cdot \text{m}^{-1}$ , respectively.

(3) The lamellar eutectic structure of alternating FCC/Laves phases plays a crucial role in dry sliding wear tests. On the one hand, the movement of a large number of dislocations in the soft FCC phase and the dislocation blockage at the soft/hard layer boundary can synergistically enhance the toughness of the coatings, and on the other hand, the layer thicknesses in the nanoscale range (<500 nm) can achieve a uniform co-deformation of the two phases, which in turn provides the lamellar eutectic structure with excellent wear-resistant properties.

#### CRediT authorship contribution statement

**Litong Feng:** Data curation. **Jinna Liu:** Investigation. **Guo Jin:** Funding acquisition. **Xiufang Cui:** Supervision. **Di Chen:** Writing – original draft, Investigation. **Xinyao Li:** Formal analysis. **Yajie Guan:** Methodology. **Zhongtao Dai:** Methodology. **Sen Ma:** Methodology, Conceptualization. **Ziyu Song:** Investigation.

#### Declaration of Competing Interest

We declare that we do not have any commercial or associative interest that represents a conflict of interest in connection with the work submitted.

#### Data Availability

No data was used for the research described in the article.

#### Acknowledgements

This work was financially supported by the National Natural Science Foundation of China (Nos. 52175163, 52275179).

#### Statement of originality

The author solemnly promises that the paper is an original paper. All or part of the text has never been published in any other publication in any form. There is no question of repeated submission, there is no plagiarism, plagiarism, no violation of laws and regulations, and Content that infringes upon the rights of others. Once it is found that the above issues are involved in the above issues, the editorial department has the right to reject the manuscript in order to maintain scientific

ethics and normal publishing order, and has the right to make real names of the paper and related authors in the field of education and scientific research as well as within the scope of brother journals. The notice criticized and has the right to notify the relevant units to impose serious administrative penalties on the main author.

## References

- [1] Wang WJ, Fu ZK, Cao X, Guo J, Liu QY, Zhu MH. The role of lanthanum oxide on wear and contact fatigue damage resistance of laser cladding Fe-based alloy coating under oil lubrication condition. *Tribol Int* 2016;94:470–8.
- [2] Holmberg K, Erdemir A. Influence of tribology on global energy consumption, costs and emissions. *Friction* 2017;5:263–84.
- [3] Du Y, Pei X, Tang Z, Zhang F, Zhou Q, Wang H, et al. Mechanical and tribological performance of CoCrNiHf eutectic medium-entropy alloys. *J Mater Sci Technol* 2021;90:194–204.
- [4] Kang N, El Mansori M. A new insight on induced-tribological behaviour of hypereutectic Al-Si alloys manufactured by selective laser melting. *Tribol Int* 2020; 149.
- [5] Sajjadnejad M, Haghshenas SMS, Badr P, Setoudeh N, Hosseinpour S. Wear and tribological characterization of nickel matrix electrodeposited composites: a review. *Wear* 2021;486:7.
- [6] Jing YZ, Fang YC, Cui XF, Chen Z, Liu DC, Liu AY, et al. Study on intrinsic mechanical behavior and erosion resistance of multi-rare earth doped LaZrO coating. *Tribol Int* 2023;185.
- [7] Lu XD, Wang HM. High-temperature phase stability and tribological properties of laser clad Mo<sub>2</sub>Ni<sub>3</sub>Si/NiSi metal silicide coatings. *Acta Mater* 2004;52:5419–26.
- [8] Sheng W, Liu D, Wang HM. Microstructure and high-temperature wear behavior of laser clad Ni-Ti-Si ternary metal silicide coatings. *Surf Coat Technol* 2008;202: 2871–7.
- [9] Zhang P, Li M, Yan H, Chen J, Yu Z, Ye X. Microstructure evolution of Ni-Mo-Fe-Si quaternary metal silicide alloy composite coatings by laser cladding on pure Ni. *J Alloy Compd* 2019;785:984–1000.
- [10] Wang HM, Cao F, Cai LX, Tang HB, Yu RL, Zhang LY. Microstructure and tribological properties of laser clad Ti<sub>2</sub>Ni<sub>3</sub>Si/NiTi intermetallic coatings. *Acta Mater* 2003;51:6319–27.
- [11] Yeh J-W, Lin S-J, Chin T-S, Gan J-Y, Chen S-K, Shun T-T, et al. Formation of simple crystal structures in CuCoNiCrAlFeTiV alloys with multiprincipal metallic elements. *Metall Mater Trans A* 2004;35:2533–6.
- [12] Cantor B, Chang ITH, Knight P, Vincent AJB. Microstructural development in equiatomic multicomponent alloys. *Mater Sci Eng: A* 2004;375-377:213–8.
- [13] Stepanov ND, Yurchenko NY, Skibin DV, Tikhonovsky MA, Salishchev GA. Structure and mechanical properties of the AlCr<sub>x</sub>NbTiV ( $x = 0, 0.5, 1, 1.5$ ) high entropy alloys. *J Alloy Compd* 2015;652:266–80.
- [14] Gao X, Lu Y, Zhang B, Liang N, Wu G, Sha G, et al. Microstructural origins of high strength and high ductility in an AlCoCrFeNi<sub>2.1</sub> eutectic high-entropy alloy. *Acta Mater* 2017;141:59–66.
- [15] Guan Y, Cui X, Li J, Zhao Y, Su W, Feng L, et al. Enhancement of grain boundary carburization of FeCoCrNiMn high-entropy alloy coating by supersonic fine particle bombardment and rare earth. *Mater Today Commun* 2023;35:106207.
- [16] Lu Y, Dong Y, Guo S, Jiang L, Kang H, Wang T, et al. A promising new class of high-temperature alloys: eutectic high-entropy alloys. *Sci Rep* 2014;4.
- [17] Xu Q, Chen D, Tan C, Bi X, Wang Q, Cui H, et al. NbMoTiVSi refractory high entropy alloys strengthened by forming BCC phase and silicide eutectic structure. *J Mater Sci Technol* 2021;60:1–7.
- [18] Chung DH, Lee J, He QF, Kim YK, Lim KR, Kim HS, et al. Hetero-deformation promoted strengthening and toughening in BCC rich eutectic and near eutectic high entropy alloys. *J Mater Sci Technol* 2023;146:1–9.
- [19] Wen X, Cui X, Liu Y, Zhang Y, Tian H, Wan S, et al. A novel strategy for promoting corrosion and wear resistance of Mg-Li alloys: gradient eutectic high-entropy alloy coating induced by in-situ bidirectional diffusion. *J Magnes Alloy* 2023.
- [20] Vo TD, Tran B, Tieu AK, Wexler D, Deng G, Nguyen C. Effects of oxidation on friction and wear properties of eutectic high-entropy alloy AlCoCrFeNi<sub>2.1</sub>. *Tribol Int* 2021;160.
- [21] Vo TD, Tieu AK, Wexler D, Su L, Nguyen C, Deng G. Fabrication and characterization of a low-cost Co-free Al<sub>0.8</sub>CrFeNi<sub>2.2</sub> eutectic high entropy alloy based solid self-lubricating composite: Microstructure, mechanical and wear properties. *J Alloy Compd* 2022;928:167087.
- [22] Vo TD, Tieu AK, Wexler D, Su L, Nguyen C, Yang J, et al. High temperature tribological performance of a cost-effective eutectic high entropy alloy Al<sub>0.8</sub>CrFeNi<sub>2.2</sub>: Comparison with AlCoCrFeNi<sub>2.1</sub>. *Tribol Int* 2023;184:108445.
- [23] Huo W, Zhou H, Fang F, Zhou X, Xie Z, Jiang J. Microstructure and properties of novel CoCrFeNiTa<sub>x</sub> eutectic high-entropy alloys. *J Alloy Compd* 2018;735: 897–904.
- [24] Du Y, Pei X, Tang Z, Zhang F, Zhou Q, Wang H, et al. Mechanical and tribological performance of CoCrNiHf<sub>x</sub> eutectic medium-entropy alloys. *J Mater Sci Technol* 2021;90:194–204.
- [25] Liu YL, Zhang F, Huang ZY, Zhou Q, Ren Y, Du Y, et al. Mechanical and dry sliding tribological properties of CoCrNiNb medium-entropy alloys at room temperature. *Tribol Int* 2021;163.
- [26] Deng G, Tieu AK, Lan X, Su L, Wang L, Zhu Q, et al. Effects of normal load and velocity on the dry sliding tribological behaviour of CoCrFeNiMoo<sub>2</sub> high entropy alloy. *Tribol Int* 2020;144:106116.
- [27] Chanda B, Potnis G, Jana PP, Das J. A review on nano-/ultrafine advanced eutectic alloys. *J Alloy Compd* 2020;827.
- [28] Zhan X, Ernst F. Crystallization micro-mechanism of near-eutectic amorphous Ni-P. *Acta Mater* 2016;104:274–82.
- [29] Wen X, Cui X, Jin G, Liu Y, Zhang Y, et al. Corrosion and tribo-corrosion behaviors of nano-lamellar Ni<sub>1.5</sub>CrCoFe<sub>0.5</sub>Mo<sub>0.1</sub>Nb<sub>x</sub> eutectic high-entropy alloy coatings: The role of dual-phase microstructure. *Corros Sci* 2022;201:110305.
- [30] Zhang L, Lu Y, Amar A, Chen X, Ren Z, Wang T, et al. Designing Eutectic High-Entropy Alloys Containing Nonmetallic Elements. *Adv Eng Mater* 2022;24: 2200486.
- [31] Guan Y, Chen D, Cui X, Li J, Feng L, Li X, et al. A novel W/FeCoCrNi-based in-situ formed high-entropy alloy gradient coating with Laves-FCC dual-phase structure and synergistic friction behavior. *Tribol Int* 2024;192:109228.
- [32] Wen X, Cui X, Jin G, Liu Y, Zhang Y, Fang Y. In-situ synthesis of nano-lamellar Ni<sub>1.5</sub>CrCoFe<sub>0.5</sub>Mo<sub>0.1</sub>Nb<sub>x</sub> eutectic high-entropy alloy coatings by laser cladding: Alloy design and microstructure evolution. *Surf Coat Technol* 2021;405.
- [33] Ding ZY, He QF, Wang Q, Yang Y. Superb strength and high plasticity in laves phase rich eutectic medium-entropy-alloy nanocomposites. *Int J Plast* 2018;106: 57–72.
- [34] Shuang S, Ding ZY, Chung D, Shi SQ, Yang Y. Corrosion resistant nanostructured eutectic high entropy alloy. *Corros Sci* 2020;164.
- [35] Shi P, Li Y, Wen Y, Li Y, Wang Y, Ren W, et al. A precipitate-free AlCoFeNi eutectic high-entropy alloy with strong strain hardening. *J Mater Sci Technol* 2021;89: 88–96.
- [36] Guo S, Liu CT. Phase stability in high entropy alloys: Formation of solid-solution phase or amorphous phase. *Prog Nat Sci: Mater Int* 2011;21:433–46.
- [37] Takeuchi A, Inoue A. Classification of bulk metallic glasses by atomic size difference, heat of mixing and period of constituent elements and its application to characterization of the main alloying element. *Mater Trans* 2005;46:2817–29.
- [38] Kim MJ, Kang GC, Hong SH, Park HJ, Mun SC, Song G, et al. Understanding microstructure and mechanical properties of (AlTa<sub>0.76</sub>)<sub>x</sub>CoCrFeNi<sub>2.1</sub> eutectic high entropy alloys via thermo-physical parameters. *J Mater Sci Technol* 2020;57: 131–7.
- [39] Chanda B, Das J. An assessment on the stability of the eutectic phases in high entropy alloys. *J Alloy Compd* 2019;798:167–73.
- [40] Lu J, Weng Y, Wan A, Sui X, Hu J, Huang C. Unveiling the effect of Si on the microstructure and properties of AlFeCoCrNi high entropy alloy coating. *J Therm Spray Technol* 2023;32:2250–61.
- [41] Zhang X, Cui X, Qi M, Zhang Q, Qi Y, Jin G. Corrosion and passivation behavior of in-situ TiC reinforced Al<sub>0.1</sub>GrNbSi<sub>0.1</sub>TaTiV refractory high entropy alloy coatings via doping C. *Corros Sci* 2024;227:111736.
- [42] Jiang L, Cui X, Jin G, Tian Z, Wen X, Tian H, et al. Design and characterization of a novel Cu<sub>2.3</sub>Al<sub>1</sub>.3Ni<sub>1</sub>.7SnCr<sub>0.3</sub> multi-principal element alloy coating on magnesium alloy by laser cladding. *J Mater Sci Technol* 2023;152:220–36.
- [43] Chandrakar R, Kumar A, Chandraker S, Rao KR, Chopkar M. Microstructural and mechanical properties of AlCoCrCuFeNiSi<sub>x</sub> ( $x = 0$  and 0.9) high entropy alloys. *Vacuum* 2021;184.
- [44] Powles RC, McKenzie DR, Meure SJ, Swain MV, James NL. Nanoindentation response of PEEK modified by mesh-assisted plasma immersion ion implantation. *Surf Coat Technol* 2007;201:7961–9.
- [45] Guan Y, Cui X, Chen D, Su W, Zhao Y, Li J, et al. Realizing high strength and toughness of gradient high-entropy alloy coating by in-situ interface reaction of FeCoCrNi/FeCoCrAl. *Surf Coat Technol* 2023;464:129569.
- [46] Maity T, Prashanth KG, Balci Ö, Wang Z, Jia YD, Eckert J. Plastic deformation mechanisms in severely strained eutectic high entropy composites explained via strain rate sensitivity and activation volume. *Compos Part B: Eng* 2018;150:7–13.
- [47] Guan Y, Zhang C, Cui X, Chen D, Li J, Li X, et al. The gradient high entropy alloy coating prepared in-situ by bidirectional diffusion of Mo/Nb and FeCoCrNi. *Surf Coat Technol* 2023;474:1430105.
- [48] Rainforth WM, Leonard AJ, Perrin C, Bedolla-Jacuinde A, Wang Y, Jones H, et al. High resolution observations of friction-induced oxide and its interaction with the worn surface. *Tribol Int* 2002;35:731–48.
- [49] Huang Y, Hu Y, Zhang M, Mao C, Tong Y, Zhang J, et al. On the enhanced wear resistance of laser-clad CoCrCuFeNiTix high-entropy alloy coatings at elevated temperature. *Tribol Int* 2022;174:107767.
- [50] Joseph J, Haghdiari N, Shamleye K, Hodgson P, Barnett M, Fabijanic D. The sliding wear behaviour of CoCrFeMnNi and Al<sub>x</sub>CoCrFeNi high entropy alloys at elevated temperatures. *Wear* 2019;428:429:32–44.
- [51] Cheng X, Jiang Z, Kosasih B, Wu H, Luo S, Jiang L. Influence of Cr-rich oxide scale on sliding wear mechanism of ferritic stainless steel at high temperature. *Tribology Lett* 2016;63:28.
- [52] Scharf TW, Prasad SV, Kotula PG, Michael JR, Robino CV. Elevated temperature tribology of cobalt and tantalum-based alloys. *Wear* 2015;330-331:199–208.
- [53] Nguyen C, Tieu AK, Deng G, Wexler D, Tran B, Vo TD. Study of wear and friction properties of a Co-free CrFeNiAl<sub>0.4</sub>Ti<sub>0.2</sub> high entropy alloy from 600 to 950 °C. *Tribol Int* 2022;169:107453.
- [54] Lu Y, Gao X, Jiang L, Chen Z, Wang T, Jie J, et al. Directly cast bulk eutectic and near-eutectic high entropy alloys with balanced strength and ductility in a wide temperature range. *Acta Mater* 2017;124:143–50.
- [55] Zhang JY, Zhang X, Wang RH, Lei SY, Zhang P, Niu JJ, et al. Length-scale-dependent deformation and fracture behavior of Cu/X (X=Nb, Zr) multilayers: the constraining effects of the ductile phase on the brittle phase. *Acta Mater* 2011;59: 7368–79.
- [56] Ding ZY, He QF, Chung D, Yang Y. Evading brittle fracture in submicron-sized high entropy intermetallics in dual-phase eutectic microstructure. *Scr Mater* 2020;187: 280–4.

- [57] Zhou Q, Zhang S, Wei X, Wang F, Huang P, Xu K. Improving the crack resistance and fracture toughness of Cu/Ru multilayer thin films via tailoring the individual layer thickness. *J Alloy Compd* 2018;742:45–53.
- [58] Deng G, Chong Y, Su L, Zhan L, Wei P, Zhao X, et al. Mechanisms of remarkable wear reduction and evolutions of subsurface microstructure and nano-mechanical properties during dry sliding of nano-grained Ti6Al4V alloy: a comparative study. *Tribol Int* 2022;169:107464.
- [59] Demkowicz MJ, Beyerlein IJ. The effects of nanoscale confinement on the behavior of metal laminates. *Scr Mater* 2020;187:130–6.
- [60] Chen X, Kong J, Li J, Feng S, Li H, Wang Q, et al. High-strength AlCoCrFeNi2.1 eutectic high entropy alloy with ultrafine lamella structure via additive manufacturing. *Mater Sci Eng: A* 2022;854:143816.
- [61] Jiang J, Zhang A, Han J, Xin B, Meng J. Investigation of microstructure and tribological properties of CoFeNi<sub>1.5</sub>VZr<sub>x</sub> eutectic high entropy alloys optimized by tuning Zr content. *Tribol Int* 2024;191:109154.
- [62] Geng Y, Chen J, Tan H, Cheng J, Zhu S, Yang J. Tribological performances of CoCrFeNiAl high entropy alloy matrix solid-lubricating composites over a wide temperature range. *Tribol Int* 2021;157:106912.
- [63] Zhao W, Yu K, Ma Q, Song C, Xiao G, Zhang H, et al. Synergistic effects of Mo and in-situ TiC on the microstructure and wear resistance of AlCoCrFeNi high entropy alloy fabricated by laser cladding. *Tribol Int* 2023;188:108827.
- [64] Pei X, Du Y, Hao X, Wang H, Zhou Q, Wu H, et al. Microstructure and tribological properties of TiZrV0.5Nb0.5Alx refractory high entropy alloys at elevated temperature. *Wear* 2022;488–489:204166.
- [65] Pole M, Sadeghilardjani M, Shittu J, Ayyagari A, Mukherjee S. High temperature wear behavior of refractory high entropy alloys based on 4-5-6 elemental palette. *J Alloy Compd* 2020;843:156004.
- [66] Geng Y, Chen J, Tan H, Cheng J, Yang J, Liu W. Vacuum tribological behaviors of CoCrFeNi high entropy alloy at elevated temperatures. *Wear* 2020;456–457:203368.
- [67] Poulia A, Georgatis E, Lekatou A, Karantzalis A. Dry-sliding wear response of MoTaWNbV high entropy alloy. *Adv Eng Mater* 2017;19:1600535.
- [68] Wei Q, Zhang A, Han J, Xin B, Su B, Wang X, et al. Development of a Ti<sub>30</sub>Hf<sub>20</sub>Nb<sub>20</sub>Ta<sub>10</sub>V<sub>10</sub>Mo<sub>7</sub>W<sub>3</sub> refractory high entropy alloy with excellent mechanical properties and wear resistance. *J Alloy Compd* 2023;966:171571.
- [69] Deng G, Tieu AK, Su L, Wang P, Wang L, Lan X, et al. Investigation into reciprocating dry sliding friction and wear properties of bulk CoCrFeNiMo high entropy alloys fabricated by spark plasma sintering and subsequent cold rolling processes: Role of Mo element concentration. *Wear* 2020;460–461:203440.
- [70] Vo TD, Deng G, Tieu AK, Su L, Wu X, Nguyen C, et al. Excellent tribological performance at elevated temperatures and associated mechanisms of novel AlCoCrFeNi-MoS<sub>2</sub> solid self-lubricating composite. *Tribol Int* 2023;189:109011.
- [71] Geng Y, Cheng J, Tan H, Sun Q, Chen J, Zhu S, et al. A (CrFeNi)83(AlTi)17 high-entropy alloy matrix solid-lubricating composite with exceptional tribological properties over a wide temperature range. *J Mater Sci Technol* 2023;153:75–91.
- [72] Cheng Z, Yang L, Huang Z, Wan T, Zhu M, Ren F. Achieving low wear in a  $\mu$ -phase reinforced high-entropy alloy and associated subsurface microstructure evolution. *Wear* 2021;474–475:203755.
- [73] Nguyen C, Tieu AK, Deng G, Wexler D, Vo TD, Wang L, et al. Tribological performance of a cost-effective CrFeNiAl<sub>0.3</sub>TiO<sub>3</sub> high entropy alloy based self-lubricating composite in a wide temperature range. *Tribol Int* 2022;174:107743.
- [74] Geng Y, Tan H, Wang L, Tieu AK, Chen J, Cheng J, et al. Nano-coupled heterostructure induced excellent mechanical and tribological properties in AlCoCrFeNi high entropy alloy. *Tribol Int* 2021;154:106662.
- [75] Yu Y, He F, Qiao Z, Wang Z, Liu W, Yang J. Effects of temperature and microstructure on the tribological properties of CoCrFeNb<sub>x</sub> eutectic high entropy alloys. *J Alloy Compd* 2019;775:1376–85.
- [76] Wang J, Han B, Chen Z, Hu C, Zhang Q, Wang C. Study on tribological oxide mechanism of CoCrFeNiMo high entropy alloy. *Wear* 2023;526–527:204907.